RESEARCH ARTICLE | SEPTEMBER 27 2011

Room temperature single-mode terahertz sources based on intracavity difference-frequency generation in quantum cascade lasers

Q. Y. Lu; N. Bandyopadhyay; S. Slivken; Y. Bai; M. Razeghi

Appl. Phys. Lett. 99, 131106 (2011)
https://doi.org/10.1063/1.3645016

APPLIED PHYSICS LETTERS 99, 131106 (2011)

Room temperature single-mode terahertz sources based on intracavity difference-frequency generation in quantum cascade lasers

Q. Y. Lu, N. Bandyopadhyay, S. Slivken, Y. Bai, and M. Razeghi[a)]

The terahertz (THz) spectral range (k¼30 300 lm) has a number of applications in biological engineering and security.[1] Being a non-ionizing radiation, it is environmentally friendly, enabling a safer exposure than conventional x-ray based techniques. However, this spectral range suffers from the lack of high performance compact sources at room temperature. Cryogenic cooling is still necessary for the operation of GaAs-based THz quantum cascade lasers (QCLs).[2,3] The recently developed THz sources based on intracavity difference-frequency generation (DFG) (Refs. 4 and 5) in dual-wavelength QCLs were able to operate at room temperature but with a 300 nW output power and a broad spectrum (0.5-1 THz). Improvement on the THz power and single mode operation is desirable for practical applications.

For the nonlinear intracavity DFG, the THz emission with a wavelength k is coherently generated in a dualwavelength (k_1 and k_2) mid-infrared (mid-IR) QCL with giant second-order nonlinear susceptibility jv$^{(2)}$j.[4–6] The THz power W is given by the following equation:

$$W ¼ \frac{p^2}{2\,0c} \; X \; \left| v^{ð2Þ}_{i;j} \right|^2 \frac{W_i W_j}{n_i n_j n_{i;j} k^2_{i;j} S_{eff}} \; l_{coh}^2; \quad (1)$$

where i, j stand for wavelength components in k_1 and k_2, respectively. l_{coh} ¼1/[jk_i k_j k_{ij}j^2 þ(a_{ij}/2)^2]$^{1/2}$ is the coherence length, W_i, n_i, k_i are the mid-IR power at a specific wavelength, refractive index, and wave vector for wavelength k_i. k_{ij} ¼1/(1/k_i 1/k_j), n_{ij} ¼n(k_{ij}), k_{ij} ¼k(k_{ij}), and a_{ij} ¼a(k_{ij}) is the THz wavelength, refractive index, wave vector, and loss, respectively. S_{eff} is the effective area of interaction.[4]

In a typical multimode Fabry-Pe´rot (FP) cavity, the light intensity spreads out among different frequencies, and the total power is the sum over many small W_i components. As such, the product W_iW_j can be small if both pumps are spectrally broad. The ideal pumping sources for DFG are two high-power, monochromatic light beams efficiently interacting within the cavity. Spectral purity in these sources is highly desirable to achieve a singular high power product in the given sum. This leads to a narrow-linewidth spectrum and high power conversion efficiency (g¼W/W_1W_2). In this work, we use an integrated dual-period distributed feedback (DFB) grating to purify the mid-IR spectra from a high power QCL. Room temperature THz emission with a narrow linewidth of 6.6 GHz is obtained with a maximum power of 8.5 lW and a conversion efficiency of g¼10 lW/W^2.

The QCL structure was grown by gas-source molecular beam epitaxy on a n-InP substrate (Si, 1.510^{17} cm^3). The growth started with a 5-lm InP buffer layer (Si, 1.510^{16} cm^3). The laser cores consisted of 30 stages of bound-to-continuum structures designed for the wavelength of k_1 9.4 lm, a 100-nm InGaAs spacer (Si, 110^{16} cm^3), and 30 stages of double-phonon resonance structure designed for the wavelength of k_2 10.8 lm.[7] The bound-to-continuum section also featured a giant nonlinear susceptibility of jv$^{(2)}$j¼410^4 pm/ V for DFG. The growth ended with a 3.5-lm InP cladding layer (Si, 1.510^{16} cm^3) and a 200-nm InP contact layer (Si, 510^{18} cm^3). Compared with Ref. 5, the lower doping levels in the waveguide reduced the losses in mid-IR and THz for about 20% and 40%, respectively. With refractive indices of n_1 ¼3.19, n_2 ¼3.13, and n¼3.6 for k_1, k_2, and k, respectively, a phase mismatch of 7 cm^1 is calculated. Combined with an estimated THz loss of 150 cm^1 gives a coherence length, l_{coh}, of approximately 120 lm, which is improved compared to the one used in Ref. 5.

Double exposure holographic lithography (HL) was used to define the dual-period DFB grating for both mid-IR and THz spectral purifications. Figure 1(a) shows the simulated superpositioned HL interferograms with equal-dose double exposures. The Fourier analysis gives clean spectra at the two wavelengths as shown in Fig. 1(b). However, as it is difficult to accurately reproduce the photo resist profile with anisotropic dry etching processing, the pattern was simply truncated into binaryequivalent square-shaped structures when transferred into SiO_2 mask, as shown in Fig. 1(a). The corresponding Fourier analysis (Fig. 1(b)) shows that besides the two main peaks, there are some satellite peaks more than 50 cm^1 away from the two main peaks due to the truncation of the interferogram. Nevertheless, laser oscillation is unlikely to occur at the position of

these satellite peaks due both to poor overlap with the laser gain curve and weaker diffractive coupling to the laser cavity.

a)
Electronic mail: razeghi@eecs.northwestern.edu.

0003-6951/2011/99(13)/131106/3/$30.00 99, 131106-1

Center for Quantum Devices, Department of Electrical Engineering and Computer Science,
Northwestern University, Evanston, Illinois 60208, USA

(Received 1 September 2011; accepted 9 September 2011; published online 27 September 2011)

We demonstrate room temperature single-mode THz emission at 4 THz based on intracavity difference-frequency generation from mid-infrared dual-wavelength quantum cascade lasers. An integrated dual-period distributed feedback grating is defined on the cap layer to purify both mid-infrared pumping wavelengths and in turn the THz spectra. Single mode operation of the pumping wavelengths results in a single-mode THz operation with a narrow linewidth of 6.6 GHz. A maximum THz power of 8.5 lW with a power conversion efficiency of 10 lW/W^2 is obtained at room temperature. Vc 2011 American Institute of Physics. [doi:10.1063/1.3645016]

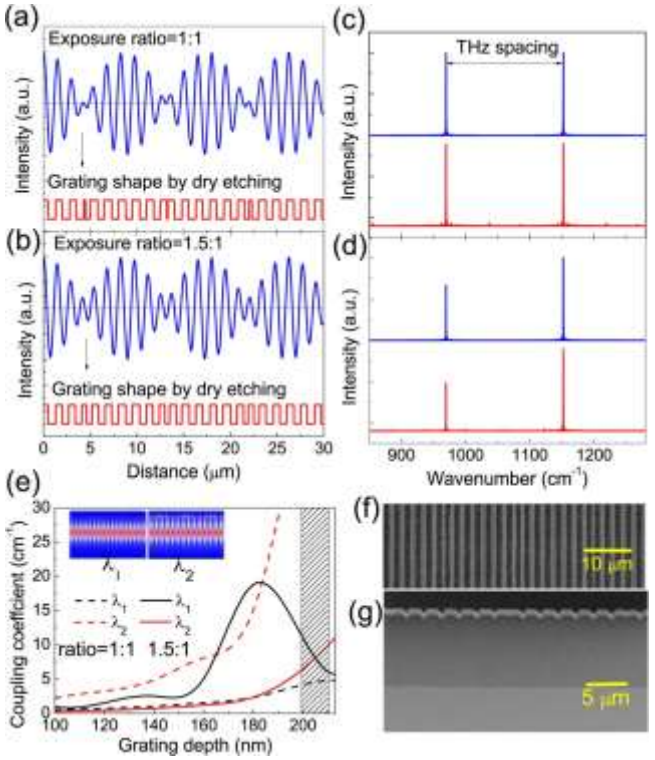

FIG. 1. (Color online) Superpositioned HL interferograms with exposure dose ratio of 1:1 (a) and 1.5:1 (c) and the truncated square gratings after dry etching. (b) and (d) Frequency analyses of the interferograms and truncated gratings in (a) and (c). (e) Coupling coefficients of the truncated gratings in (a) and (c) with different grating depths. The shaded region is the targeted grating depth. The insets in (e) are two eigenmodes for the dual-period grating. (f) and (g) SEM images of dual-period grating in SiO_2 hard mask after RIE (top view) and the grating shape after ICP etching and top Ti/Au contact deposition (cross-sectional view).

Figure 1(e) shows the calculated coupling coefficients (j_1 for k_1 and j_2 for k_2) for the case of equal exposure intensity. Clearly, j_1 is much smaller than j_2. This is because the longer wavelength k_2 has a more expanded mode profile (see the inset of Fig. 1(e)) and has a stronger interaction with the surface gratings than the shorter wavelength k_2. To obtain similar coupling coefficients, the grating shape is reconstructed by changing the dose ratio of the two exposures with a similar strategy as in Ref. 8. The HL interferograms with a dose ratio of 1.5:1, the truncated grating profile, and the corresponding frequency analyses are shown in Figs. 1(c) and 1(d). Around a grating depth of 200 nm (shaded region in Fig. 1(e)), the coupling coefficients of these two wavelengths are similar (6–10 cm^1). This design offers sufficient coupling strength for 2-3 mm cavities with highreflection (HR) coatings. Figures 1(f) and 1(g) are the scanning electron microscope (SEM) images of the SiO_2 mask after the reactive-ion etching (RIE) and the grating shape after inductively coupled plasma (ICP) etching and top Ti/Au contact deposition.

The sample was processed into double-channel geometries with a 16-lm ridge width tapered into 60 lm with taper angles (h) varying from 1-2.3. A dual-period surface grating as designed above was defined into the cap layer with a grating depth of 200 nm, following the similar description in Ref. 9. For comparison, an FP counterpart was processed. A 400-nm Si_3N_4 layer was used for electrical insulation. 2–3 mm cavities were cleaved and HR coated with Y_2O_3/Au on the back facet and mounted epilayer-up on copper heat sinks.

All testing was performed at room temperature in pulsed mode operation, with a pulse width of 60 ns and a duty cycle of 1.5%. Mid-IR peak power was obtained from the average power measured with a calibrated thermopile detector divided by duty cycle. THz emission power was collected by a Golay cell detector in an ambient condition. Two 3 in. diameter parabolic mirrors with focal lengths of 2 and 6 in. were used to collect light from the laser and focus in onto the detector. A high-resistivity hyperhemispherical Si lens with 3-mm diameter and 1.8-mm height was used following a similar setup in Ref. 10. The alignment of the Si lens was checked by an infrared camera. THz power was corrected by a collection efficiency of 50% considering the limited collecting aperture (10 mm) of the Golay cell detector. Optical filters were used to differentiate the THz power from mid-IR powers. Spectra measurement for mid-IR and THz signals were performed on a Bruker Fourier transform infrared (FTIR) spectrometer with a mercury-cadmium-telluride (MCT) detector and liquid helium cooled silicon bolometer, respectively. Far fields were obtained with a computer controlled rotational stage and a MCT detector.

Figures 2(a) and 2(b) show the measured mid-IR and THz spectra for a 2-mm long DFB device with a taper angle of 2.3 at room temperature. Single mode emission around 4 THz (k 73.9 lm) is obtained for the DFB device (Fig. 2(b)) due to single mode operation of the two pumping sources shown in Fig. 2(a). In contrast, the FP device emits a broadband multi-wavelength THz spectrum due to the multimode operation of the mid-IR sources. The linewidth of the THz

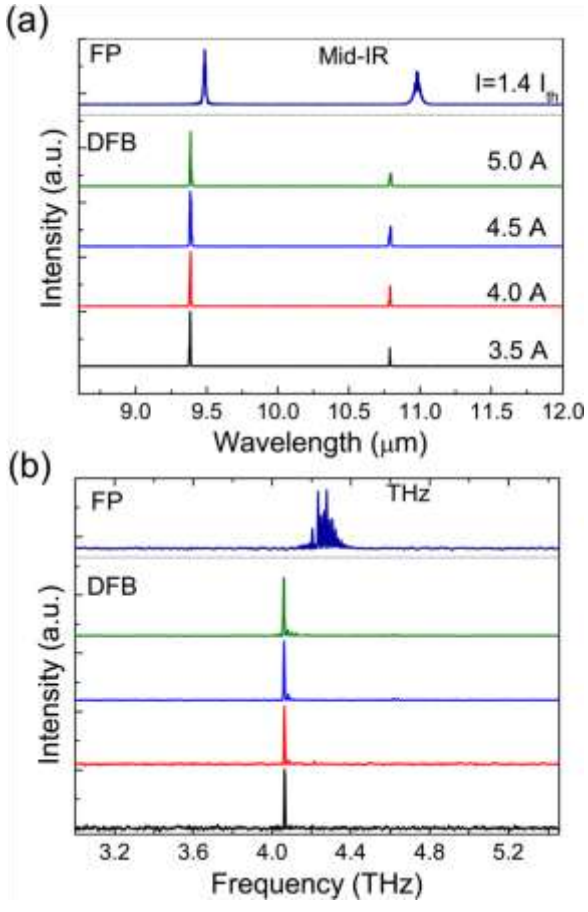

FIG. 2. (Color online) Room temperature mid-IR (a) and THz (b) spectra at different currents of a 2-mm-long DFB device and its FP counterpart with a taper angle of 2.3. I_{th} is the threshold current of the FP device.

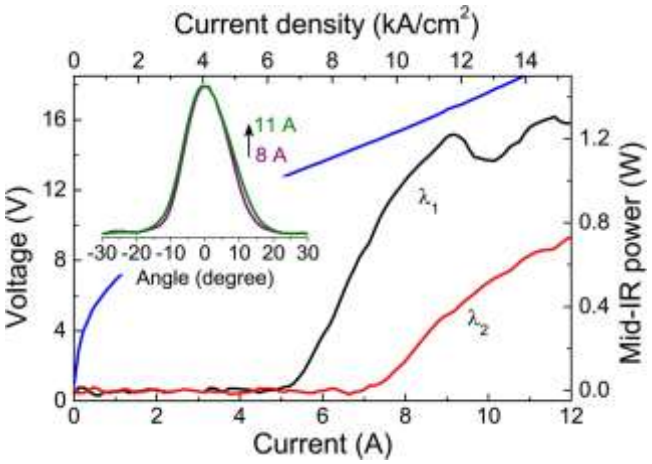

FIG. 3. (Color online) Room temperature mid-IR P-I-V characteristics for a 3-mm-long DFB device with a taper angle of 1. The inset is the total-power far field distributions for the two wavelengths at low current (I¼8 A) and high current (I¼11 A), respectively.

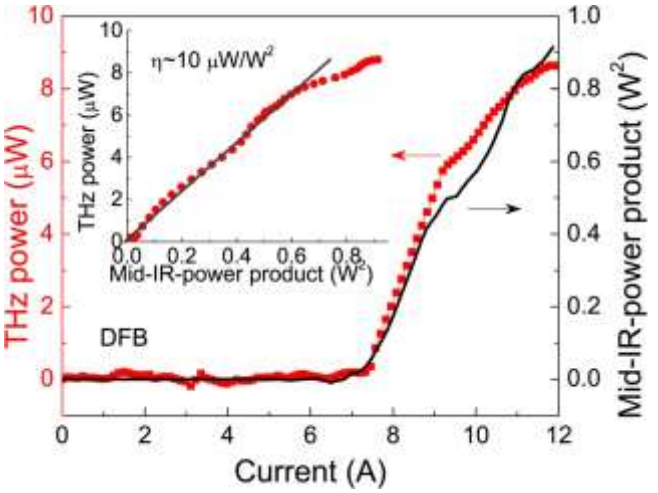

FIG. 4. (Color online) Room temperature THz peak power and mid-IR-power product characteristics for a 3-mm-long DFB device with a taper angle of 1. The inset is the THz peak powers as a function of the mid-IR-power product. The THz power conversion efficiency is deduced from a linear fit.

signal from the DFB device is 6.6 GHz, which is mainly limited by the resolution 3.75 GHz (0.125 cm^{1}) of FTIR. Interestingly, the wavelength is nearly constant at different currents, with a significantly smaller current-tuning coefficient of 1.5 GHz/A compared to the mid-IR pumping signals (11.4 GHz/A). This is expected because the wavelength tuning for DFB lasers is determined by the change of refractive index as a function of temperature. Since the two mid-IR wavelengths are close to each other, their refractive indices change at a similar rate as a function of temperature. As a result, the THz difference frequency signal has about one order of magnitude smaller tuning rate than the corresponding mid-IR signals.

Figure 3 shows the mid-IR power-current-voltage (P-I-V) characteristics for 3-mm long DFB devices with a taper angle of 1 at room temperature. The maximum mid-IR peak power of the DFB device is around 1.2 and 0.8 W for the two wavelength, which is about half of the FP device. The insets in Fig. 3 are the total-power far field distributions for the two wavelengths at low and high currents. The device maintains a fundamental transverse mode operation in the working currents as seen from the single-lobed far-field distribution with negligible beam steering for the two wavelengths. The slight broadening at high current (I¼11 A) can be explained by the self-focusing effect caused by the nonlinear response of the refractive index to the intense optical field.[9]

Figure 4 shows the THz power and mid-IR-power product for the DFB device at room temperature. A maximum THz peak power of 8.5 lW is obtained. The insets show the THz power as a function of the mid-IR-power product. The THz power conversion efficiency for the DFB device is about 10 lW/W^2 for all working currents. Compared with Ref. 5, the improved power conversion efficiency for the DFB device results from the improved coherence length and purified spectra. The FP counterpart delivers a maximum THz peak power of 13 lW with a conversion efficiency of 10 lW/W^2 near threshold and rapidly decreasing to 3.5 lW/W^2 toward the power rollover of the midIR signal. The reduced conversion efficiency is attributed to spectral broadening and spatial-hole burning at high currents.

In conclusion, we demonstrate room temperature THz emission at 4 THz from dual-period DFB QCLs based on intracavity DFG. The wavelength of the THz signal is very constant for different currents with a narrow linewidth of 6.6 GHz. A maximum THz power of 8.5 lW with a high power conversion efficiency of 10 lW/W^2 is obtained, benefiting from low midIR and THz losses, high mid-IR pumping powers, and single mode operation of the mid-IR pumping sources. Widely tunable, narrow linewidth THz sources are also achievable by incorporating technologies of dual-period DFB array[11] or individually pumped double-DFB elements merged in a Y-shaped amplifier. In view of much more efficient and powerful mid-IR pump designs at shorter wavelengths around 4.5–5 lm,[12] intracavity DFG with a dual-period DFB grating in this wavelength range may be a viable technology to boost the THz output power to the mW-level at room temperature.

The authors would like to thank the support, interest, and encouragement of Dr. Tariq Manzur from the Naval Undersea Warfare Center and Dr. Scott Rodgers from Defense Advanced Research Projects Agency.

1 M. Tonouchi, Nat. Photonics 1, 97 (2007).
2 R. Ko¨hler, A. Tredicucci, F. Beltram, H. E. Beere, E. H. Linfield, A. G. Davies, D. A. Ritchie, R. C. Iotti, and F. Rossi, Nature 417, 156 (2002).
3 S. Kumar, Q. Hu, and J. L. Reno, Appl. Phys. Lett. 94, 131105 (2009).
4 M. A. Belkin, F.Capasso, A. Belyanin, D. L. Sivco, A. Y. Cho, D. C. Oakley, C. J. Vineis, and G. W. Turner, Nat. Photonics 1, 288 (2007).
5 M. A. Belkin, F. Capasso, F. Xie, A. Belyanin, M. Fischer, A. Wittmann, and J. Faist, Appl. Phys. Lett. 92, 201101 (2008).
6 Y. R. Shen, The Principles of Nonlinear Optics (Wiley, New York, 1984).
7 J. Faist, D. Hofstetter, M. Beck, T. Aellen, M. Rochat, and S. Blaser, IEEE J. Quantum Electron. 38, 533 (2002).
8 Q. Y. Lu, W. Zhang, L. Wang, J. Liu, L. Li, F. Q. Liu, and Z. Wang, Opt. Express 17, 18900 (2009).
9

Q. Y. Lu, Y. Bai, N. Bandyopadhyay, S. Slivken, and M. Razeghi, Appl. Phys. Lett. 98, 181106 (2011).
10 A. W. M. Lee, Q. Qin, S. Kumar, B. S. Williams, Q. Hu, and J. L. Reno,Opt. Lett. 32, 2840 (2007).
11 B. G. Lee, M. A. Belkin, R. Audet, J. MacArthur, L. Diehl, C. Pflugl, D.C. Oakley, D. Chapman, A. Napoleone, D. Bour, S. Corzine, G. Hofler, J. Faist, and F. Capasso, Appl. Phys. Lett. 91, 231101 (2007).
12 Y. Bai, N. Bandyopadhyay, S. Tsao, S. Slivken, and M. Razeghi, Appl. Phys. Lett. 98, 181102 (2011).